Title: The onset of nucleate boiling prediction in a mini channel with the Eulerian multiphase flow

Authors: K. Han, B. Hardy

Corresponding Author: K. Han

Email:kai.han@srnl.doe.gov

Tel.: +1-803-725-0083

Mailing Address: Savannah River Site, Building 773-41A, Aiken SC 29808 USA

Author information:

Savannah River National Laboratory

Savannah River Site, Aiken SC 29808 USA

Kai Han, Bruce Hardy

Title: The onset of nucleate boiling prediction in a mini channel with the Eulerian multiphase flow

Authors: K. Han and B. Hardy

Abstract

The prediction of boiling incipience is a critical issue for a reactor. Vapor lock causes operating instability and undesirable temperature rise, especially for small channels. This study uses the Eulerian multiphase flow boiling model to predict the onset of nucleate boiling in a millimeter scale rectangular channel. Two wall boiling models, namely the RPI (Rensselaer Polytechnic Institute) and the non-equilibrium subcooled model are applied. Computational fluid dynamics is employed for this study to investigate the impact of operating conditions like liquid flow rate, operating pressure, heat flux, velocity profile, turbulence model, and inlet liquid temperature. The effect of fundamental boiling parameters on the surface wall temperature and vapor volume fraction is also studied. The parameters under consideration are the bubble departure diameter, bubble departure frequency, nucleate site density, quenching time period, and interface heat transfer coefficients. A series of CFD calculations is conducted by varying the considered variables systematically in a wide range of flow conditions covering laminar, transition, and turbulent flows. The sub-component heat fluxes like the liquid convective, the vapor convective, the evaporative, and the quenching terms are monitored to infer the boiling dynamics in the transition region from the single-phase flow to the nucleate boiling zone. It is found that the CFD approach to detecting the boiling incipience point agrees reasonably with available experimental data. However, its limitations, like inaccuracy for lower flow rates and early transition to boiling flow, are also noticed due to the nature of the considered RPI model.

keywords: ONB, Eulerian multiphase flow, Nucleate Boiling, Mini channel, CFD, RPI model

1. INTRODUCTION

Nucleate boiling is an efficient method for transport of heat away from a heated surface through the phase change process. Boiling that occurs when the bulk liquid temperature is below its saturation temperature is known as subcooled nucleate boiling, and it is a highly efficient convective heat transfer process. However, it is generally desired to avoid two-phase flow in some thermal systems like a nuclear research reactor because generated bubbles may form a vapor film that can lead to flow instability and, consequently, surface damage. Therefore, a prediction of the first location where active nucleation sites occur is a critical issue.

One crude approximation is that the onset of nucleate boiling (ONB) may occur either before or after the intersection point of the single-phase liquid forced convective curve and the fully developed nucleate boiling curve [1]. Several classical ONB estimation correlations were presented in terms of heat flux and operating pressure, such as the model by Bergles and Rohsenow [2]. They developed a model similar to the semi-theoretical model proposed by Hsu's [3] nucleation model in the thermal boundary layer having a temperature gradient. This model is convenient to use when wall temperature is known or when a considered problem has a relatively simple function of wall superheat, heat flux, and operating pressure. Wang et al. [4] conducted various experimental methods for ONB detection in a narrow rectangular channel which has a vertical upward flow. They noticed that pressure drops and heat transfer coefficients show convex patterns as mass flux increases for a fixed heat flux. As a wall boiling develops, a rapid increase in the channel pressure drop and heat transfer coefficient is observed for increased heat flux at a constant mass flux. They also reported no significant discrepancies occurring in detecting ONB among the experimental techniques described above. Additionally, it was found that wall superheat at the inception of boiling is dependent on the inlet subcooling, heat flux, and mass flux. In their

experiments with an internal combustion engine cooling system, Castiglione et al. [5] observed that the slope of the wall temperature with respect to coolant mass flow rate changes from a linear to exponential increase as the mass flow rate is decreased and the single-phase flow transitions to two-phase flow.

Unlike the single-phase flow, the multi-phase flow calculations are computationally expensive, complex, and not always successfully analyzed with CFD. However, CFD still has benefits over the experimental approach in terms of cost, safety, convenience when handling variables/geometry change, isolation of specific phenomena, capability to deal with extreme operating conditions, etc. Various CFD methods have been utilized in the area of multiphase flow. For example: bubble behavior influenced by low frequency vibration under reduced gravity was studied in the pool boiling regime using the volume of fluid [6] method. Liquid droplet evaporation in the air stream was modeled in a spray cooling system using the discrete phase model coupled with turbulent flow [7]. Departure from the nucleate boiling regime was predicted using the RPI (Rensselaer Polytechnic Institute) model [8], and ONB was estimated in a small rectangular channel using the PRI model [9].

Even though Al-Yahia and Jo [9] demonstrated the possibility of using CFD to detect ONB, a systematic study is still needed for the influence of fundamental parameters on prediction of ONB. These parameters include interface heat transfer coefficient, bubble departure diameter, bubble departure frequency, nucleation site density, operating pressure, quenching period time, grid density, and the turbulence model that is employed.

In the study presented in this paper, the impact of the aforementioned parameters on ONB is investigated with regards to the RPI and the non-equilibrium subcooled boiling models (NEB) by comparing model results with available experimental data. Various thermo-hydraulic parameters

are monitored and controlled with the assistance of CFD. The Eulerian multiphase flow model, integrated with the wall boiling models (RPI and NEB), is utilized in a wide range of flow regimes from laminar, transition, and turbulent flows.

2. NUMERICAL METHOD

2.1 Eulerian multi-phase flow equations

Subcooled boiling is the physical situation where boiling occurs on the heated wall even though the bulk liquid temperature is lower than the saturation temperature. The thermal energy transfer from the heated wall to the liquid increases the liquid temperature and eventually generates vapor. Interphase heat transfer between the liquid and vapor increases liquid temperature while condensing vapor. The Eulerian multiphase flow model solves the conservation equations for phase continuity, momentum, and energy along with a turbulence model. Wall boiling is commonly modeled by using the RPI [10] model and with the non-equilibrium subcooled boiling model [11], developed by Lavieville et al. [11] for the Departure from Nucleate Boiling (DNB).

The continuity equation for Eulerian multiphase flow is expressed as

$$\frac{\partial}{\partial t}\left(\alpha_q \rho_q\right) + \nabla \cdot \left(\alpha_q \rho_q \vec{v}_q\right) = \sum_{p=1}^{n}(\dot{m}_{pq} - \dot{m}_{qp}) \quad (1)$$

The conservation of momentum for a fluid phase q is

$$\frac{\partial}{\partial t}\left(\alpha_q \rho_q \vec{v}_q\right) + \nabla \cdot \left(\alpha_q \rho_q \vec{v}_q \vec{v}_q\right) = -\alpha_q \nabla \mathrm{p} + \nabla \cdot \bar{\bar{\tau}}_q + \alpha_q \rho_q \vec{g} + \sum_{p=1}^{n}[K_{pq}(\vec{v}_p - \vec{v}_q) + \dot{m}_{pq}\vec{v}_{pq} - \dot{m}_{qp}\vec{v}_{qp}] + (\vec{F}_q + \vec{F}_{td,q}) \quad (2)$$

Considering the minor amount of vapor formation near the wall at ONB condition, the lift force, the wall lubrication force, and the virtual mass force are excluded. The lift force is negligible because the vapor phase does not separate from the wall quickly at ONB conditions. For the same reason, the wall lubrication force, that pushes the vapor phase away from the walls, is excluded. The virtual mass force is essential when the vapor phase accelerates relative to the liquid phase

and deflects the surrounding liquid. Hence, it is not necessary to include these contributions to the conservation of momentum equation.

In this model, the vapor phase is assumed to form bubbles. The momentum exchange coefficient is expressed in the following form.

$$K_{pq} = \frac{\rho_p f_d}{6\tau_p} d_p A_i \tag{3}$$

where, $f_d = \frac{C_D \mathrm{Re_r}}{24}$ and C_D is based on the universal drag law [12]. d_p is bubble diameter and $\mathrm{Re_r}$ is the relative Reynolds number.

The turbulent dispersion force arises from turbulent diffusion and drives the vapor away from the vicinity of the wall towards the center of the pipe. For this effect, the Lopez de Bertodano model [13] is adopted.

$$\vec{F}_{td,q} = \rho_q k_q \nabla \alpha_p \tag{4}$$

A separate enthalpy equation for the q^{th} phase can be written as:

$$\frac{\partial}{\partial t}\left[\alpha_q \rho_q \left(e_q + \frac{\vec{v}_q^2}{2}\right)\right] + \nabla \cdot \left[\alpha_q \rho_q \vec{v}_q \left(h_q + \frac{\vec{v}_q^2}{2}\right)\right] = \nabla \cdot \left(\alpha_q k_{eff,q} \nabla T_q + \bar{\bar{\tau}}_{eff,q} \cdot \vec{v}_q\right) + \sum_{p=1}^{n} (Q_{pq} + \dot{m}_{pq} h_{pq} - \dot{m}_{qp} h_{qp}) + p \frac{\partial \alpha_q}{\partial t} + S_q \tag{5}$$

The intensity of heat exchange between the p and q phases (Q_{pq}) is expressed as

$$Q_{pq} = h_{pq,i} A_i (T_p - T_q) \tag{6}$$

The volumetric heat transfer coefficient between the p^{th} phase and the q^{th} phase ($h_{pq,i}$) comes from the Ranz-Marshall model [14].

Three different Reynolds averaged Navier-Stokes turbulence models, such as the standard k-ε model, the Realizable k-ε turbulence model, and the Reynolds Stress Model (RSM) are tested with

scalable wall functions to avoid the deterioration of standard wall functions under grid refinement below the critical distance from the wall. The intention of the scalable wall function is to produce consistent results for grids using the log law with the standard wall function. The standard k-ε model [15] assumes a fully turbulent flow and the effects of molecular viscosity are negligible. The Realizable k- ε turbulence model [16] is known for good performance for separated flows and flows with complex secondary flow features among all the k-ε models. The RSM [17] is the most elaborate Reynolds Averaged Navier Stokes turbulence model. Unlike others, it includes the effect of anisotropic eddy-viscosity by solving transport equations for the Reynolds stresses. It accounts for the effects of streamline curvature, swirl, rotation, and more rapid changes in strain rate unlike the other two-equation models. Considering the Reynolds number range in this study, transition Shear Stress Transport (SST) model may be considered, especially for laminar to turbulent transition flows. However, the transition models (three or four equation models) have not validated in multiphase flow. Additionally, they require very fine mesh (y^+ <1) and the Eulerian multiphase flow wall boiling model does not work with this mesh requirement.

The default turbulence model in this study is the standard k-ε mixture model.

The transport equations for k and ε in the standard k-ε model are

$$\frac{\partial}{\partial t}(\rho_m k) + \nabla \cdot (\rho_m k \vec{v}_m) = \nabla \cdot \left[\left(\mu_m + \frac{\mu_{t,m}}{\sigma_k}\right)\nabla k\right] + G_{k,m} - \rho_m \varepsilon + \Pi_{k_m} \quad (7)$$

$$\frac{\partial}{\partial t}(\rho_m \varepsilon) + \nabla \cdot (\rho_m \varepsilon \vec{v}_m) = \nabla \cdot \left[\left(\mu_m + \frac{\mu_{t,m}}{\sigma_\varepsilon}\right)\nabla \cdot \varepsilon\right] + \frac{\varepsilon}{k}\left(C_{1\varepsilon} G_{k_m} + C_{2\varepsilon}\rho_m \varepsilon\right) + \Pi_{\varepsilon_m} \quad (8)$$

where, the turbulent viscosity, $\mu_{t,m}$, molecular viscosity, μ_m, velocity, $\vec{v}_m$, the volume fraction, α, the production of turbulence kinetic energy, $G_{k,m}$, and source, Π. The dilatation dissipation term,

which addresses the effect of compressibility, is negligible in this study due to the low flow speed and operating pressure. Hence, it is not included in the *k* equation.

The model constants have the following values.

$$C_{1\varepsilon} = 1.44,\ C_{2\varepsilon} = 1.92,\ C_{\mu} = 0.09,\ C_{3\varepsilon} = -0.33,\ \sigma_k = 1.0,\ \sigma_{\varepsilon} = 1.3$$

The total heat flux ($\dot{q}_w$) from the wall to the liquid in the RPI model is composed of the convective heat flux ($\dot{q}_C$), the quenching heat flux ($\dot{q}_Q$), and the evaporative heat flux ($\dot{q}_E$).

$$q"_W = q"_C + q"_Q + q"_E \tag{9}$$

The convective heat flux is the function of the single-phase heat transfer coefficient (h_c) and the area of influence (A_b).

$$q"_C = h_c(T_w - T_l)(1 - A_b) \tag{10}$$

The quenching heat flux represents the cyclic averaged transient energy transfer by liquid filling the wall vicinity after bubble detachment.

$$q"_Q = C_w \frac{2k_l}{\sqrt{\pi \lambda_l T_p}}(T_w - T_l)A_b \tag{11}$$

where k_l is the conductivity, T_p is the quenching periodic time, and λ_l is the diffusivity. C_w is a coefficient to correct the waiting time between departures of consecutive bubbles.

The evaporative flux is expressed by the volume of the bubble, the active nucleation site density, vapor density, the latent heat, and the bubble departure frequency.

$$q"_E = V_d N_w \rho_v h_{lv} f \tag{12}$$

where V_d is the volume of the bubble based on the bubble departure diameter, N_w is the active nucleate site density, h_{lv} is the latent heat of evaporation, and f is the bubble departure frequency.

The frequency of bubble departure has the following form [18].

$$f = \sqrt{\frac{4g(\rho_l - \rho_v)}{3\rho_l D_w}} \tag{13}$$

The nucleate site density is the function of wall superheat [19].

$$N_w = 210^{1.805}(T_w - T_{sat})^{1.805} \tag{14}$$

The bubble departure diameter is based on empirical correlations [20]. For the bubble departure frequency and the nucleate site density modification, ANSYS Fluent submodel, DEFINE_BOILING_PROPERTY was used as a user defined function.

$$D_w = \min\left(0.0014, \frac{0.0006e^{-\Delta T_{sub}}}{45}\right) \tag{15}$$

The RPI model fixes the vapor temperature at saturation temperature. It needs to include the vapor temperature to model DNB or the critical heat flux. The non-equilibrium subcooled boiling model (NEB) has the vapor phase convective heat flux.

$$q"_W = \left(q"_C + q"_Q + q"_E\right)f(\alpha_l) + [1 - f(\alpha_l)]q"_V \tag{16}$$

The convective heat flux of the vapor phase is expressed as follows.

$$q"_V = h_V(T_w - T_V) \tag{17}$$

The function $f(\alpha_l)$ depends on the local liquid volume fraction [11].

2.2 Numerical setup

A two-dimensional rectangular channel having a 2.5 mm height and 566 mm length is constructed as Fig. 1 to conform with the experimental setup [9]. It has a velocity inlet that has a uniform velocity profile and a pressure outlet. A uniform heat flux boundary condition is applied between 133 mm and 433 mm along the flow direction on one side. The other wall boundaries are set as an adiabatic condition. Gravity acts in the opposite direction of the flow to depict a vertical upward flow.

Various meshes are prepared to investigate the grid sensitivity to the turbulence models and the Eulerian multiphase flow model. Uniform meshes along the channel height are created while varying the number of grids. A part of a typical grid is presented in Fig. 1 along with the geometry. A finer grid near the wall is not adopted in this study because all the evaporation from the heated wall is specified in the first cell next to it, and a very fine cell cannot handle the phase change numerically. A very fine mesh having a unity of y^+ did not converge in the Eulerian multiphase flow for this numerical setup. The grid density dependency is checked in terms of heated surface wall temperature, which is the most influential parameter to enable boiling incipience. For a given operating condition (1.3 bar absolute pressure, 410 kW/m^2 heat flux, Re of 7609, and 40^{o}C inlet water temperature), no meaningful wall temperature difference with respect to grid density is detected, as shown in Fig. 2. For example, the maximum wall temperatures as grids are 106.5 K, 106.4 K, 106.7K, and 106.9 K for 5, 20, 25, and 30 meshes normal to the wall, respectively. Moreover, the ONB incipient wall heat flux was identical at 420 kW/m^2 for all meshes. Considering the heat flux step size of 10 kW/m^2, a mesh having a total of 94,100 (20 normal to the wall × 4705 along the flow passage) cells is selected. The corresponding y^+ for this mesh at Re of 7609 is 11.7 which is acceptable for the scalable wall function.

Constant thermo-physical properties from REFPROP v.10 [21] are used to obtain stabilized solutions. Liquid properties are based on the inlet condition, and the vapor properties are from a saturated temperature corresponding to its operating pressure. The operating pressure ranges between 1.0 and 1.3 bar as in the experiment [9]. The working fluid is water.

All analyses are conducted at steady state with a pressure-based solver. The coupled scheme is used for pressure-velocity coupling. The coupled algorithm solves the momentum and pressure-based continuity equations together and offers a robust and efficient performance compared to the segregated solution schemes. The Green-Gauss Node based scheme [22] and PRESTO! (PREssure STaggering Option) scheme [23] are used for gradient and pressure spatial discretization methods. Gradients are needed to construct scalar values on the cell faces and compute secondary diffusion terms and velocity derivatives. The node-based Green-Gauss scheme reconstructs exact values of a linear function at a node from surrounding cell-centered values on arbitrary unstructured meshes by solving a constrained minimization problem, preserving second-order spatial accuracy. The PRESTO! scheme uses a discrete continuity balance for a staggered control volume about the face to compute the staggered pressure. The second-order upwind scheme [24] is adopted for momentum and energy discretization. Quantities at cell faces are calculated using a multidimensional linear reconstruction approach in the seconds-order upwind scheme. In this approach, higher-order accuracy is achieved on cell faces through a Taylor series expansion of the cell-centered solution of the cell centroid. The first-order upwind scheme is introduced to volume fraction, turbulent kinetic energy, and turbulent dissipation rate discretization techniques. The first-order upwind scheme determines quantities at cell faces by assuming that the cell-center values of any field variable represent a cell-average value and hold throughout the entire cell. All simulations are initialized using the inlet boundary condition. A series of numerical analyses for

the constructed two-dimensional rectangular channel is carried out by simultaneously solving all the equations described above using commercial CFD software, Ansys Fluent 2021R1.

3. RESULTS

General boiling characteristics are presented in Fig. 2, 3, and 4 with wall temperature, heat transfer coefficients, vapor volume fraction, and heat fluxes for the NEB model. As soon as the liquid flow is exposed to the heated surface, a sudden surface temperature jump occurs as Fig. 2 shows. Conversely, an abrupt temperature drop is detected at the end of the heated surface. On the heated surface, the wall temperature gradually increases and shows a linear slope as flow proceeds and nucleation conditions become more favorable in farther downstream.

The incipient location of nucleate boiling approaches the inlet with increasing heat flux. For a 420 kW/m^2 heat flux boundary condition, a very small amount of vapor fraction (order of 10^{-23}) forms on the surface. The incipient location for each heat flux condition is 0.145 m, 0.136 m, and 0.133 m for 420 kW/m^2, 460 kW/m^2, and 500 kW/m^2 heat flux boundary conditions, respectively. It is also detected that the location of the steep gradients of vapor volume fraction on the wall is shortened with increasing heat flux. From Fig. 3, it can be seen that the surface heat transfer coefficients are much more sensitive to heat flux once nucleate boiling occurs relative to the case for single-phase flow. The ONB heat flux for the flow conditions depicted in Fig. 3 is 420 kW/m^2. In single-phase flow, which occurs below a surface heat flux of 420 kW/m^2, the change in the heat transfer coefficient with heat flux is minor. Conversely, for heat flux that exceeds 420 kW/m^2, corresponding to boiling, the dependence of the heat transfer coefficient on heat flux is discernable. This trend for heat transfer coefficients after phase change occurs is also seen in the experimental work of Wang et al. [4]. Interestingly, for single-phase flow at a fixed wall heat flux, the surface heat transfer coefficients increase in the direction of flow. In these steady state calculations, the

single-phase liquid temperature increases along the length of the flow channel, hence, the temperature difference between the surface and the liquid is reduced. This situation requires the heat transfer coefficient to increase to maintain the constant wall heat flux. Conversely, the surface heat transfer coefficient behavior in the boiling regime is opposite to that for single-phase flow due to the existence of bubbles. The lower thermal conductivity of bubbles act as an insulating layer, and the temperature difference across the bubbles accounts for a large part of the temperature difference between the heated surface and the fluid. Complicating this process, departing bubbles allow liquid back filling to reduce the temperature near the heating surface. These observations suggest that the behavior of the heat transfer coefficient in the direction of flow may serve as another indicator for ONB.

The relative contributions of liquid convection, evaporation, quenching, and vapor convection heat fluxes are presented in Fig. 4 for 420, 460, and 500 kW/m^2 total heat fluxes. Until ONB occurs (420 kW/m^2), the other heat flux components do not appear, and the liquid phase convective heat flux is the sole player in the heat transfer mechanism as the first graph of Fig. 4 shows. As soon as nucleate boiling starts, the quenching heat flux and the evaporative heat flux emerge while the liquid phase convective heat flux drops. The incipient location of nucleate boiling (vapor volume fraction) matches the quenching and evaporative heat flux starting point. Another noticeable behavior is the sudden spike of the vapor convective heat flux fraction at the nucleate boiling incipient location. After the abrupt spike, it gradually increases as the flow path. The abrupt increase in the quenching heat flux at the end of the heated surface is due to the rapid refilling of the surface by low-temperature liquid at junction with the un-heated surface and the large temperature difference between the heated wall surface and the liquid temperature. As the relative

values to the total heat flux shows, boiling related sub-components are still minor compared to that of the liquid phase convective heat flux near the ONB regime.

Heat flux is increased by 10 kW/m^2 to detect ONB for each operating condition. ONB can be detected by the presence of a vapor volume fraction near the wall or by monitoring whether the maximum surface temperature exceeds the saturation temperature corresponding to the local pressure in the Eulerian multiphase flow wall boiling models. Table 1 summarizes the comparison of results between the RPI and the NEB models. In general, the NEB model delays ONB slightly compared to the RPI model, and the Eulerian multiphase flow models predict lower ONB heat flux than the corresponding experimental measurements by Al-Yahia and Jo [9]. For laminar flow conditions (Re = 878), both models predict very low ONB heat flux as much as a 50 kW/m^2 difference. In turbulent flow, these Eulerian multiphase boiling models reasonably agree well with the experimental data [9]. However, except for transient condition from laminar to turbulent flow (Re = 2341), both models predict a lower ONB heat flux.

Hsu's [3] semi-theoretical analysis to determine the criteria for the onset of nucleate boiling provides insight into obtaining the approximate wall superheat estimation for ONB. The wall superheat at ONB occurrence, ΔT_{ONB} can be estimated for saturated liquid water by setting the following equation equal to zero.

$$\sqrt{1-\frac{12.8\sigma T_{sat}}{\rho_v h_{fv} \delta_t \Delta T_{ONB}}} = 0 \qquad (18)$$

The thermal boundary layer thickness, δ_t, is approximated by using the single-phase heat transfer coefficient and assuming a linear temperature gradient in the thermal boundary layer.

$$\delta_t = k_l / h_C \qquad (19)$$

The calculated thermal boundary layer thickness for the considered conditions varies from 0.6 mm to 85 μm. The thermal boundary layer thickness decreases with increasing Reynolds number while the heat transfer coefficients increase. The estimated ΔT_{ONB} for Reynolds numbers 878, 2341, 4552, and 7609 conditions in the experimental data of Al-Yahia and Jo [9] obtained through Hsu's method are 0.32 K, 0.88K, 1.32 K, and 2.25 K, respectively. The estimated ΔT_{ONB} using the Bergles and Rohsenow model [2], in Eq. 20, are 3.76 K, 5.52 K, 4.29 K, and 8.09 K at the ONB heat fluxes and 1.3 bar operating pressures in the experiments of Al-Yahia and Jo [9].

$$\Delta T_{ONB} = \frac{5}{9}\left[\frac{q"_{ONB}}{1082P^{1.156}}\right]^{\frac{P^{0.0234}}{2.16}} \quad (20)$$

Even though the Bergles and Rohsenow [2] model is being reported as very conservative [4], its predicted values of ΔT_{ONB} is higher than that of Hsu's [3] semi-theoretical method. As these estimations suggest, a minimum value of wall superheat is required to activate the nucleation sites. However, the Eulerian multiphase boiling models allow boiling when the liquid temperature near the wall exceeds the saturation temperature. Therefore, early boiling incipience is detected in the Eulerian multiphase boiling model at a lower heat flux than the experimental results of of Al-Yahia and Jo [9]. Therefore, further development and investigation of the Eulerian multiphase boiling flow model is required for ONB prediction.

As Bowring [1] suggests, the onset of nucleate boiling (ONB) may be approximated by the point of intersection of the single-phase liquid forced convective curve and the fully developed nucleate boiling curve. Fig. 5 compares the single-phase CFD and the Eulerian multiphase boiling model CFD results. The points of intersection are almost identical to the ONB heat fluxes given by the Eulerian multiphase boiling models. However, as seen in Table 1, for Re > 2341, the model predicts ONB at lower surface heat fluxes than does the experimental data [9]. The intersection

method may provide a quick estimation of ONB heat flux by conducting two Eulerian multiphase boiling CFD runs and two single-phase CFD runs rather calculations for step-changes in the heat flux, as examined in this paper. However, ONB is difficult to discern in the low Reynolds number region illustrated for Re = 878 and 2341 in Table 1. This is another weak area of the Eulerian multiphase flow model because the necessity for using small channels to increase heat transfer will lead to reduced flow rates restricted by large pressure drops in tiny channels. Moreover, the prediction of ONB in small channels is more critical because small amounts of vapor can easily cause vapor lock and lead to critical heat flux conditions. As described in the previous modeling section, an appropriate turbulence model may be required for the transition region from laminar to turbulent flow. The currently available turbulent flow models for the transition region require very fine grids near the wall and does not work properly with the Eulerian multiphase flow wall boiling model. Further enhancement of turbulence model in the transition flow regime along with the Eulerian multiphase flow wall boiling model is required to improve the ONB prediction accuracy.

Table 1 also shows the impact of the turbulence model on ONB prediction. The realizable k-ε and the RSM model show slightly lower ONB heat flux than the standard k-ε model for the Re = 7609 case. This work's simple flow condition does not have complex flow patterns like separation, streamline curvature, swirl, rotation, and rapid changes in strain rate. Hence, the benefits of more delicate turbulence models do not appear in this set of numerical calculations.

Velocity profile also plays a role in the temperature gradient in a channel in general. The actual experimental test section for Reference [9] has a horizontal inlet and a horizontal outlet, with the inlet at the bottom relative to the gravitational force, as shown in Fig. 6 demonstrates. For the corresponding model, a geometry similar to the experimental test section is constructed in a two-dimensional format, and a velocity profile is obtained from CFD calculations for Re = 7609 from

it. Velocity profiles at the start of the heated section (133 mm away from the inlet) are presented in Fig. 7. One is from the uniform velocity inlet setting of the geometry in Fig. 1 and the other is from Fig. 6. They are close to each other because the flow is fully developed before entering the heated zone. As expected from the close similarity of those two velocity profiles, the wall temperatures of the heated surface are almost identical, as seen in Fig. 8. As long as the channel is long enough to attain fully developed flow at the start of the heated section, a uniform velocity profile is adequate for the level of analysis in this work.

For fixed values of Re = 7609, the operating pressure of 1.3 barA, and a wall heat flux of 460 kW/m^2, the sensitivity of fundamental boiling parameters used in the Eulerian multiphase wall boiling model are investigated and summarized in Table 2. This operating condition is selected to produce nucleate boiling to investigate the impact of the individual boiling parameters. The ONB heat flux for this condition is 420 kW/m^2. Interface heat transfer coefficients ($h_{pq,i}$), bubble departure diameter (D_w), bubble departure frequency (f), nucleate site density (N_w), operating pressure (p), and quenching period time (T_p) are systemically varied. The average surface wall temperature, the maximum surface wall temperature, and the vapor volume fraction on the heated surface are monitored. Cases 2, 3, 4, 5, 6, and 7 show the impact of interface heat transfer coefficients. Surface temperatures and vapor volume fractions on the heated wall decrease with increasing the interface heat transfer coefficients because the low temperature liquid efficiently takes away heat from the vapor and condenses. The effect of bubble departure diameter is analyzed in cases 8 and 9. Larger bubble departure diameters increase the vapor volume fraction near the wall by holding bigger bubbles. Even though bubble departure frequency decreases as the bubble departure diameter increase (see equation 13), larger bubbles take more heat from the surface and thermal boundary layer disturbance by them allows low temperature liquid to rush into the site of

the departing bubble. In this way, the surface is cooled more efficiently by bigger size bubbles. As increase in the bubble departure frequency lowers the surface temperature by removing heat more efficiently and increases the vapor volume fraction near the wall because this flow is located in the relatively low Reynolds number region, and the turbulent dispersion effect is not strong enough to carry away the departed bubbles, as cases 10, 11, 12, and 13 demonstrate. The influence of nucleation site density can be observed for cases 14, 15, 16, and 17. It is natural to see a larger vapor volume fraction near the wall with increased nucleation site density. It also leads to more frequent bubble departure and consequently a reduction in the wall temperature. Because the liquid saturation temperature depends on the local pressure, elevated operating pressure allows the fluid to remain in the liquid phase up to a higher temperature and subsequently increases the surface temperature by delaying the bubble formation. Therefore, the wall heat flux for ONB is larger for a higher operating pressure. Finally, the effect of the quenching periodic time is investigated by varying the bubble waiting time coefficient in cases 20 and 21. From equation 11, increasing the bubble waiting time coefficient enhances the quenching heat flux, and decreases surface temperature by increasing the occupying time of lower temperature liquid on the wall surface. It leads to lower vapor volume fraction on the wall.

4. CONCLUSION

The onset of nucleate boiling is predicted for various flow regimes from laminar, transition, and turbulent flows using the Eulerian multiphase wall boiling models. The RPI (Rensselaer Polytechnic Institute) boiling model and its extended form, the Non-Equilibrium subcooled Boiling model (NEB), are introduced to the Eulerian multiphase flow calculation for a simple two-dimensional millimeter scale rectangular channel. The CFD results agree reasonably well with the available experimental data. However, the considered Eulerian multiphase flow model allows

boiling with lower heat flux and its applicability to lower Reynolds number regions is limited. The behavior of surface wall temperature, the location of boiling incipience, the surface heat transfer coefficient, and components of total heat flux are also investigated. The surface heat transfer coefficients increase in different directions relative to the direction of flow depending on whether the flow is single-phase or boiling flow. This behavior may be used as a tool to detect the incipience of nucleate boiling. The total heat flux is divided into sub-components, namely the liquid convective heat flux, the quenching heat flux, the evaporative heat flux, and the vapor convective heat flux. Their contributions are in good physical correspondence with the development of the vapor volume fraction along the heated surface. The impact of the velocity profile is not remarkable as long as the flow channel is long enough to have fully developed flow at the start of the heated section. Using the intersecting point between the single-phase flow and the boiling curve to detect the incipience of nucleate boiling is as accurate as the solely using the Eulerian multiphase flow boiling model, but it shares the same limitations. Even though its applicability in the low Reynolds number region is questionable and not clearly discernable, it may provide a simple and quick rough estimation method for a complex geometry using a small number of CFD runs. The effect of fundamental boiling parameters is also studied for interface heat transfer coefficient, bubble departure diameter, bubble departure frequency, nucleate site density, operating boiling pressure, and quenching time period. Even though their individual influence is presented in this work, the interaction between those parameters merits further investigations.

ACKNOWLEDGEMENTS

This work was produced by Battelle Savannah River Alliance, LLC under Contract No. 89303321CEM000080 with the U.S. Department of Energy. Publisher acknowledges the U.S.

Government license to provide public access under the DOE Public Access Plan (http://energy.gov/downloads/doe-public-access-plan).

Conflicts of interest

On behalf of all authors, the corresponding author states that there is no conflict of interest.

References

1. R. W. Bowring, 1962, Physical model based on bubble detachment and calculation of steam voidage in the subcooled region of a heated channel, OECD Halden Reactor Project Report HPR-10.
2. A. E. Bergles, and W. M. Rohsenow, 1964, The determination of forced-convection surface-boiling heat transfer, J. Heat Transfer, Vol. 86, pp. 365-372.
3. Y.. Y. Hsu, and R. W. Graham, 1961, An analytical and experimental study of the thermal boundary layer and the ebullition cycle in nucleate boiling, NASA TN-D-594.
4. C. Wang, H. Wang, S. Wang, and P. Gao, 2014, Experimental study of boiling incipience in vertical narrow rectangular channel, Annals of Nuclear Energy, Vol. 66, pp. 152-160.
5. T. Castiglione, F. Pizzonia, R. Piccione, and S. Bova, 2016, Deecting the onset of nucleate boiling in internal combustion engines, Applied Energy, Vol. 164, pp. 332-340.
6. D. Han and M. A. Kedzierski, 2017, Numerical analysis of the influence of low frequency vibration on bubble growth, Int. J. Transport Phenomena, Vol. 15, pp. 37-52.
7. D. Han, 2015, Numerical study on air temperature reduction by water spray, Int. J. Transport Phenomena, Vol. 14, pp. 205-217.

8. R. Zhang, W. Zhang, T. Cong, W. Tian, G. H. Su, and S. Qiu, 2015, Application of RPI model: Prediction of subcooled boiling and DNB in vertical pipes, 16th Int. Topical Meeting on Nuclear Reactor Thermal Hydraulics, Chicago, IL, pp. 2658-2672.
9. O. S. Al-Yahia and D. Jo, 2017, Onset of nucleate boiling for subcooled flow through a one-side heated narrow rectangular channel, Annals of Nuclear Energy, Vol. 109, pp. 30-40.
10. N. Kurul and M. Z. Podowski, 1990, Multidimensional effects in forced convection sub cooled boiling, in Proceedings of the International Heat Transfer Conference, Jerusalem, Israel.
11. J. Lavieville, E. Quemerais, S. Mimouni, M. Boucker, and N. Mechitoua, 2005, NEPTUNE CFD V1.0 Theory Manual, Internal Report EDF H-I81-2006-04377-EN.
12. N. I. Kolev, 2005, Multiphase flow dynamics 2: Thermal and Mechanical Interactions, 2nd ed., Springer, Berlin, Germany.
13. M. Lopez de Bertodano, 1991, Turbulent bubbly flow in a triangular duct, Ph.D. Thesis, Rensselaer Rolytechnic Institute, Troy, New York.
14. W. E. Ranz and W. R. Marshall, 1952, Evaporation from drops, Chem. Eng. Prog, Vol. 48, pp. 14-146.
15. B. E. Launder and D. B. Spalding, 1972, lectures in mathematical Models of Turbulence, Academic Press, London, England.
16. T. H. Shih, W. W. Liou, A. Shabbir, Z. Yang, and J. Zhu, 1995, A new k- ε Eddy-Viscosity Model for High Reynolds Number Turbulent Flows – Model Development and Validation, Computers Fluids, Vol. 24, pp. 227-238.

17. B. E. Launder, G. J. Reece, and W. Rodi, 1975, Progress in the Development of a Reynolds-Stress Closure, J. Fluid Mech., Vol. 68, pp. 537-566.
18. R. Cole, 1960, A photographic study of pool boiling in the region of the critical heat flux, AIChE Journal, Vol. 6, pp. 533-538.
19. M. Lemmert and J. Chawla, 1977, Influent of flow velocity on surface boiling heat transfer coefficient, Heat Transfer in Boiling, Vol. 237, pp. 247.
20. V. I. Tolubinski and D. M. Kostanchuk, 1970, Vapor bubbles growth rate and heat transfer intensity at subcooled water boiling, 4th International Heat Transfer Conference, Paris, France.
21. E. W. Lemmon, I. H. Bell, M. L. Huber, and M. O. McLinden, 2018, NIST Standard Reference Database 23: Reference Fluid Thermodynamic and Transport Properties-REFPROP, Version 10.0, National Institute of Standards and Technology, Standard Reference Data Program, Gaithersburg.
22. D. G. Holmes and S. D. Connell, 1989, Solution of the 2D Navier-Stokes Equations on Unstructred Adaptive Grids, AIAA 9th Computational Fluid Dynamics Conference.
23. R. Peyret, 1996, Handbook of computational fluid mechanics, San Diego, Academic Press.
24. T. J. Barth and D. Jespersen, 1989, The design and application of upwind schemes on unstructured meshes, Technical Report AIAA-89-0366, 27th Aerospace Sciences Meeting, Reno, Nevada.

NOMENCLATURE

A_b	area of influence by boiling [-]
A_i	interface surface area [m^2]
$C_{1\varepsilon}$, $C_{2\varepsilon}$, $C_{3\varepsilon}$	Standard k-ε equations constants [-]

1	C_D	drag coefficient [-]
2	c_p	specific heat [J/kg·K]
3	C_w	bubble waiting time coefficient [-]
4	d_p	particle diameter [m]
5	D_w	bubble departure diameter [m]
6	e	internal energy [m^2/s^2]
7	f	bubble departure frequency [Hz]
8	f_d	drag function [-]
9	$\vec{F}_q$	external body force [N]
10	$\vec{F}_{td,q}$	turbulent dispersion force [N]
11	$f(\alpha_l)$	local liquid volume fraction function [-]
12	$\vec{g}$	acceleration due to gravity [m/s^2]
13	G_k	generation of turbulence kinetic energy due to the mean velocity gradients [W/m^3]
14	h	enthalpy [J/kg]
15	h_C	single-phase heat transfer coefficient [W/m^2K]
16	h_{lv}	latent heat of evaporation [J/kg]
17	h_{pq}	interphase enthalpy [J/kg]
18	$h_{pq,i}$	interphase heat transfer coefficient [W/m^2K]
19	h_V	vapor-phase heat transfer coefficient [W/m^2K]
20	k	turbulent kinetic energy [J/kg]
21	k_{eff}	effective conductivity [W/m·K]
22	k_l	thermal conductivity of liquid [W/mK]
23	K_{pq}	momentum exchange coefficient between p^{th} phase and q^{th} phase [kg/s]

1	$\dot{m}_{pq}$	mass transfer from phase p to phase q [kg/s]
2	$\dot{m}_{qp}$	mass transfer from phase q to phase p [kg/s]
3	N_w	nucleate site density [-]
4	p	pressure [Pa]
5	Q_{pq}	intensity of heat exchange between the p^{th} and q^{th} phases [N/m^{2}s]
6	$q"_C$	convective heat flux [W/m^2]
7	$q"_E$	evaporative heat flux [W/m^2]
8	$q"_Q$	quenching heat flux [W/m^2]
9	$q"_W$	total heat flux from the wall to the liquid [W/m^2]
10	Re	Reynolds number [-]
11	Re_r	relative Reynolds number [-]
12	S_q	source term [J/s]
13	T	temperature [K]
14	T_p	quenching periodic time [s]
15	t	time [s]
16	V_d	volume of the bubble based on the bubble departure diameter [m^3]
17	$\vec{v}$	velocity vector [m/s]
18	y^+	dimensionless quantity for the distance from the wall [-]
19	*Greek letters*	
20	α	volume [m^3]
21	δ_t	thermal boundary layer thickness [m]
22	ε	turbulent dissipation rate [m^2/s^3]
23	μ	dynamic viscosity [Pa·s]

1	μ_t	turbulent viscosity [Pa·s]
2	Π_ε	source term for ε [kg/s^{4}m]
3	Π_k	source term for k [W/m^3]
4	ρ	density [kg/m^3]
5	σ	surface tension [N/m]
6	σ_ε	turbulent Prandtl number for ε [-]
7	σ_k	turbulent Prandtl number for k [-]
8	τ_p	particulate relaxation time [s]
9	$\bar{\bar{\tau}}_{eff}$	effective stress tensor [Pa]
10	$\bar{\bar{\tau}}_q$	q^{th} phase stress-strain tensor [Pa]
11	*Subscripts*	
12	ave	average
13	eff	effective
14	in	inlet
15	l	liquid phase
16	m	mixture
17	max	maximum
18	p	pth phase
19	q	qth phase
20	sat	saturation
21	sub	subcooling
22	v	vapor phase

List of Tables

Table 1 Comparison of RPI and NEB models at 1.3 bar absolute pressure (107.11°C saturation temperature)

Re	T_{in} [°C]	Turbulence model	$\dot{q}_{ONB}$ [kW/m^2] by experiment	$\dot{q}_{ONB}$ [kW/m^2] by PRI	$\dot{q}_{ONB}$ [kW/m^2] by NEB
878	40	Standard	89	40	40
2341	40	Standard	117	140	150
4552	55	Standard	203	190	190
7609	40	Standard	462	410	420
7609	40	Realizable	462	370	400
7609	40	RSM	462	400	400

Table 2 Boiling parameter impact at 1.3 bar absolute pressure (107.11°C saturation temperature)

Case No	$h_{pq,i}$ [W/m^{2}K]	D_w [m]	f [Hz]	N_w	p [barA]	C_w [-]	T_{max} [°C]	T_{ave} [°C]	α_V
1	[14]	[20]	[18]	[19]	1.3	1	113.1	111.5	3.35E-07
2	0	[20]	[18]	[19]	1.3	1	119.7	111.7	7.82E-03
3	1.0E+01	[20]	[18]	[19]	1.3	1	116.3	111.6	4.60E-03
4	1.0E+02	[20]	[18]	[19]	1.3	1	113.2	111.5	5.62E-04
5	1.0E+03	[20]	[18]	[19]	1.3	1	113.2	111.6	4.77E-05
6	1.0E+04	[20]	[18]	[19]	1.3	1	113.2	111.6	4.70E-06
7	1.0E+05	[20]	[18]	[19]	1.3	1	113.2	111.6	4.67E-07
8	[14]	0.0001	[18]	[19]	1.3	1	113.6	111.9	1.81E-07
9	[14]	0.001	[18]	[19]	1.3	1	109.1	108.3	5.40E-06
10	[14]	[20]	1	[19]	1.3	1	114.7	112.6	5.72E-10
11	[14]	[20]	10	[19]	1.3	1	114.7	112.6	1.54E-08
12	[14]	[20]	100	[19]	1.3	1	114.5	112.5	1.49E-07
13	[14]	[20]	1000	[19]	1.3	1	113.4	111.7	1.16E-06
14	[14]	[20]	[18]	1.0E+04	1.3	1	114.4	112.4	4.30E-09
15	[14]	[20]	[18]	1.0E+05	1.3	1	114.4	112.4	1.17E-07
16	[14]	[20]	[18]	1.0E+06	1.3	1	114.1	112.2	1.17E-06
17	[14]	[20]	[18]	5.0E+06	1.3	1	113.3	112.1	5.86E-06
18	[14]	[20]	[18]	[19]	1.1	1	113.8	112.0	1.54E-06
19	[14]	[20]	[18]	[19]	1.2	1	113.8	112.0	8.33E-07
20	[14]	[20]	[18]	[19]	1.3	0.1	113.9	112.0	6.09E-07
21	[14]	[20]	[18]	[19]	1.3	1.0E+01	110.6	109.7	1.32E-07

List of figures

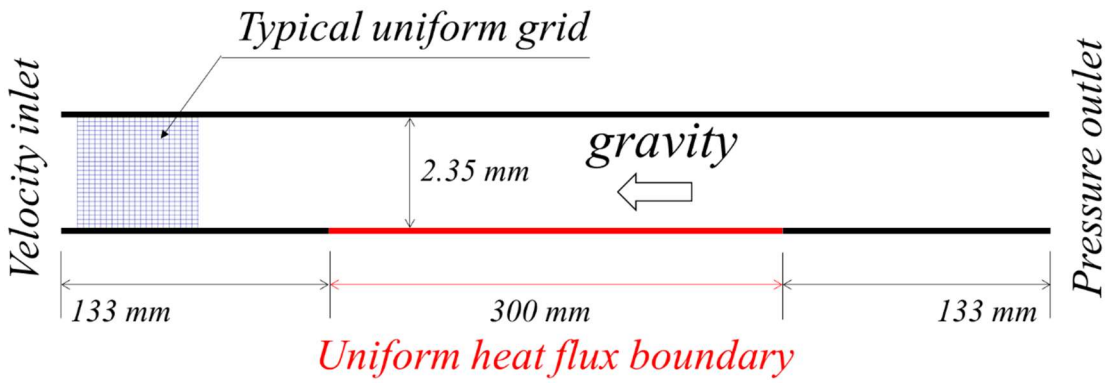

Fig. 1 Geometry with boundary conditions

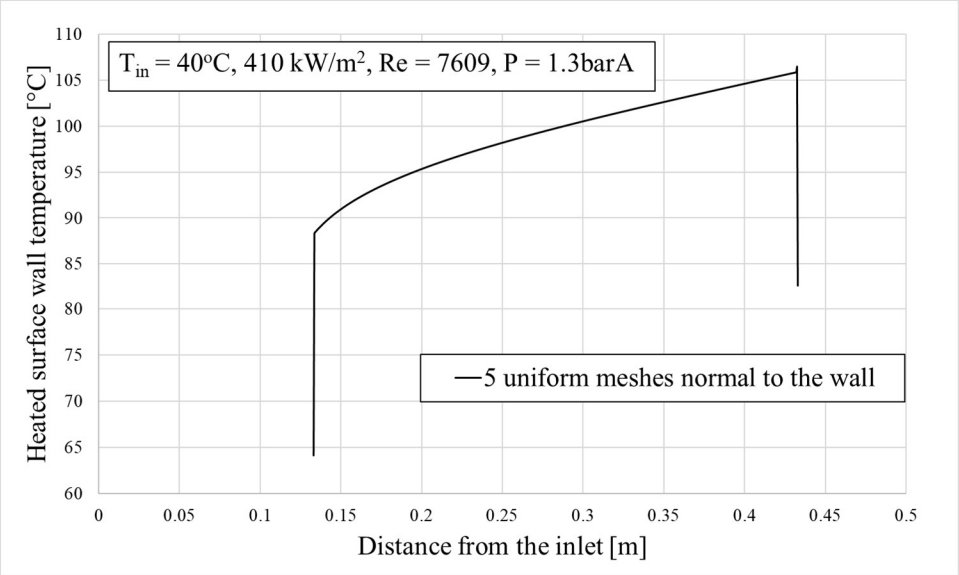
T_{in} = 40°C, 410 kW/m², Re = 7609, P = 1.3barA
—5 uniform meshes normal to the wall
Heated surface wall temperature [°C]
Distance from the inlet [m]
110
105
100
95
90
85
80
75
70
65
60
0
0.05
0.1
0.15
0.2
0.25
0.3
0.35
0.4
0.45
0.5

1

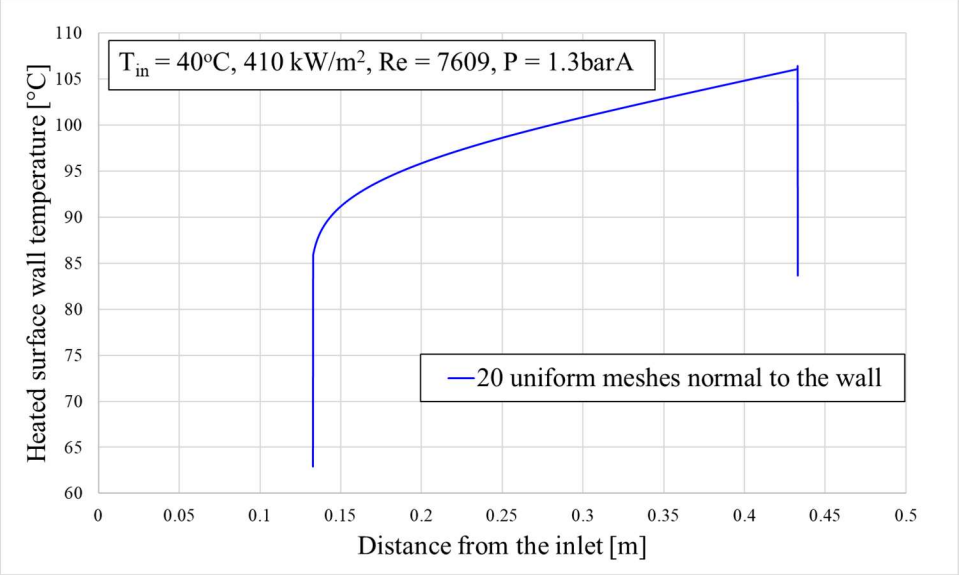
T_{in} = 40°C, 410 kW/m², Re = 7609, P = 1.3barA
—20 uniform meshes normal to the wall
Heated surface wall temperature [°C]
Distance from the inlet [m]
110
105
100
95
90
85
80
75
70
65
60
0
0.05
0.1
0.15
0.2
0.25
0.3
0.35
0.4
0.45
0.5

2

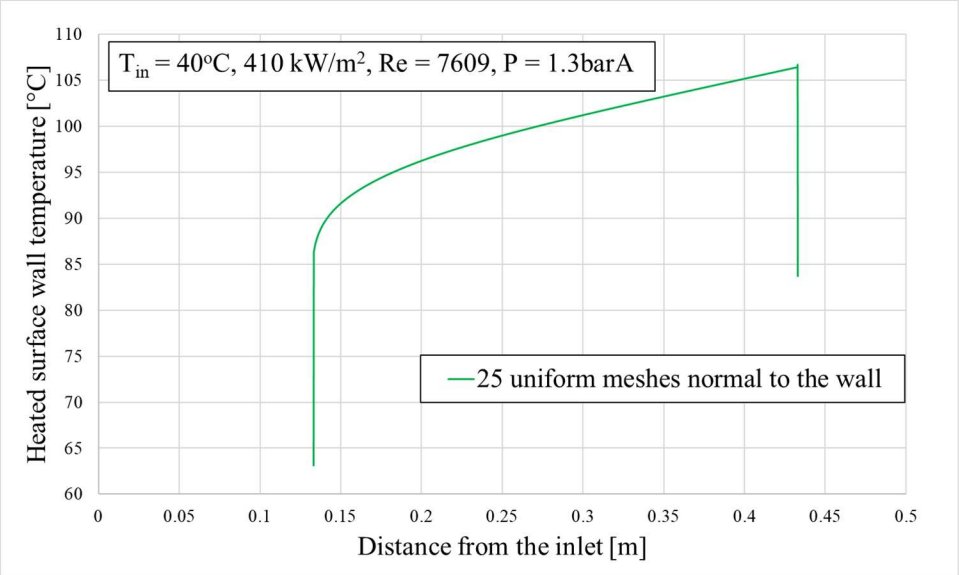

1

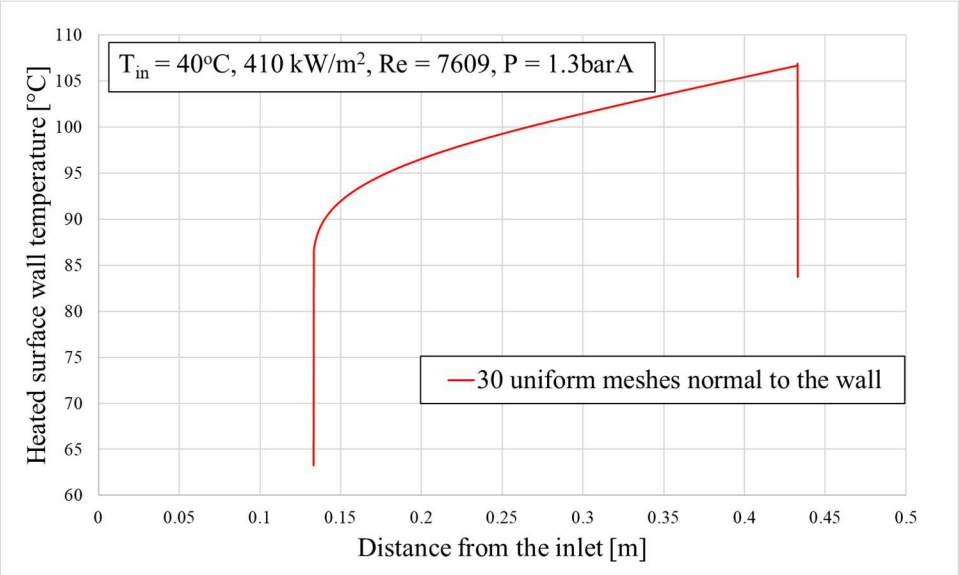

2

3 Fig. 2 Grid dependency

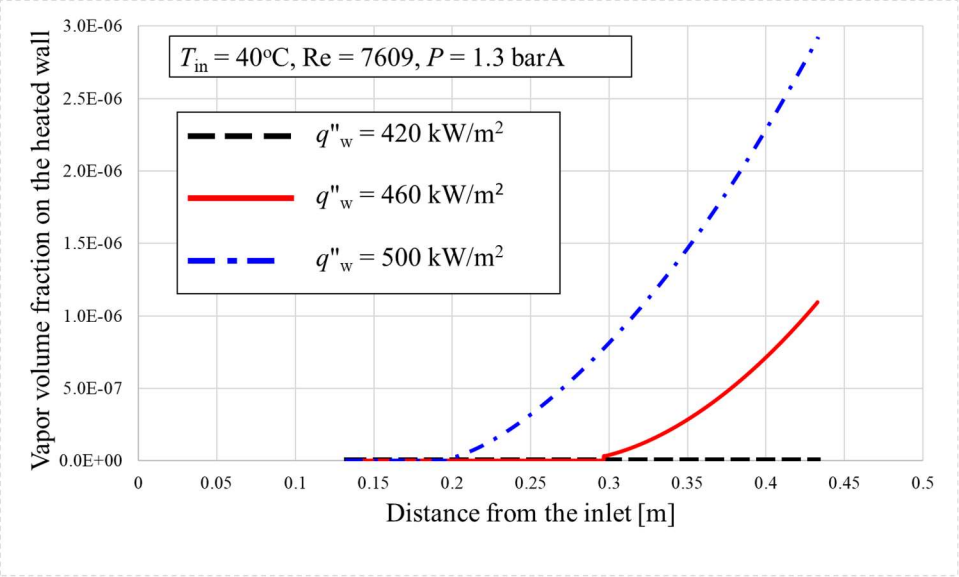

(a) Vapor volume fraction on the heated wall

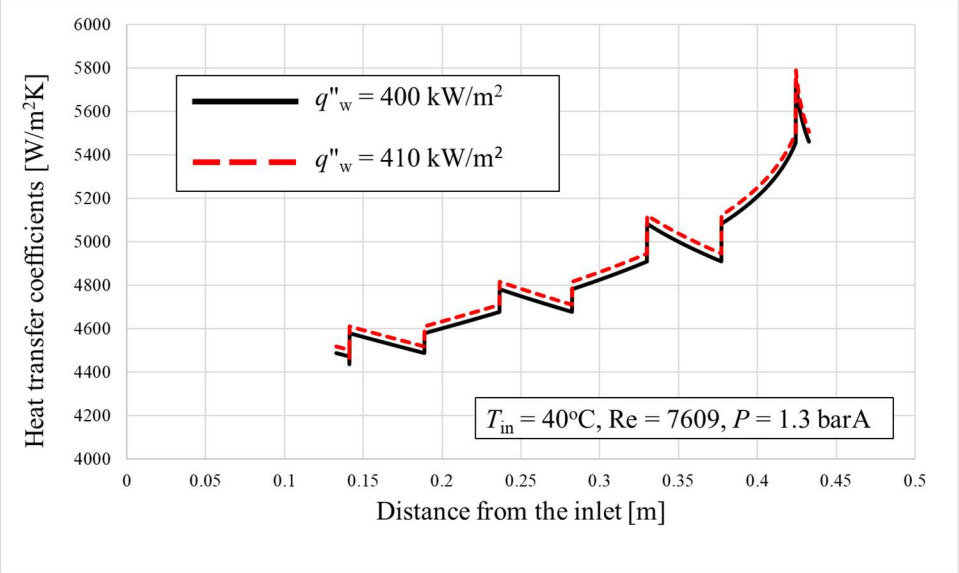

(b) Heat transfer coefficients on the heated wall for single-phase flow mode

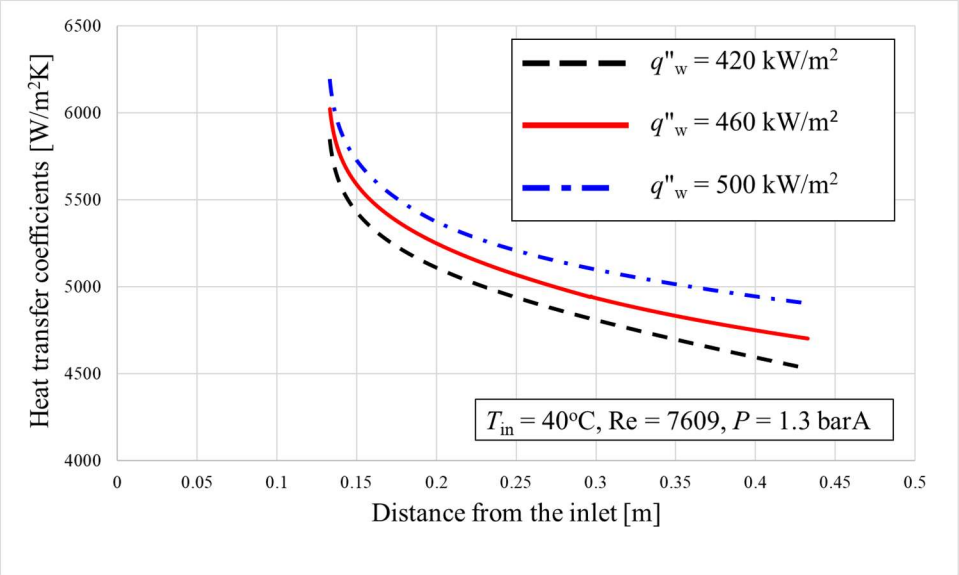

(c) Heat transfer coefficients on the heated wall for boiling mode

Fig. 3 Vapor volume fraction and surface heat transfer coefficients on the heated wall

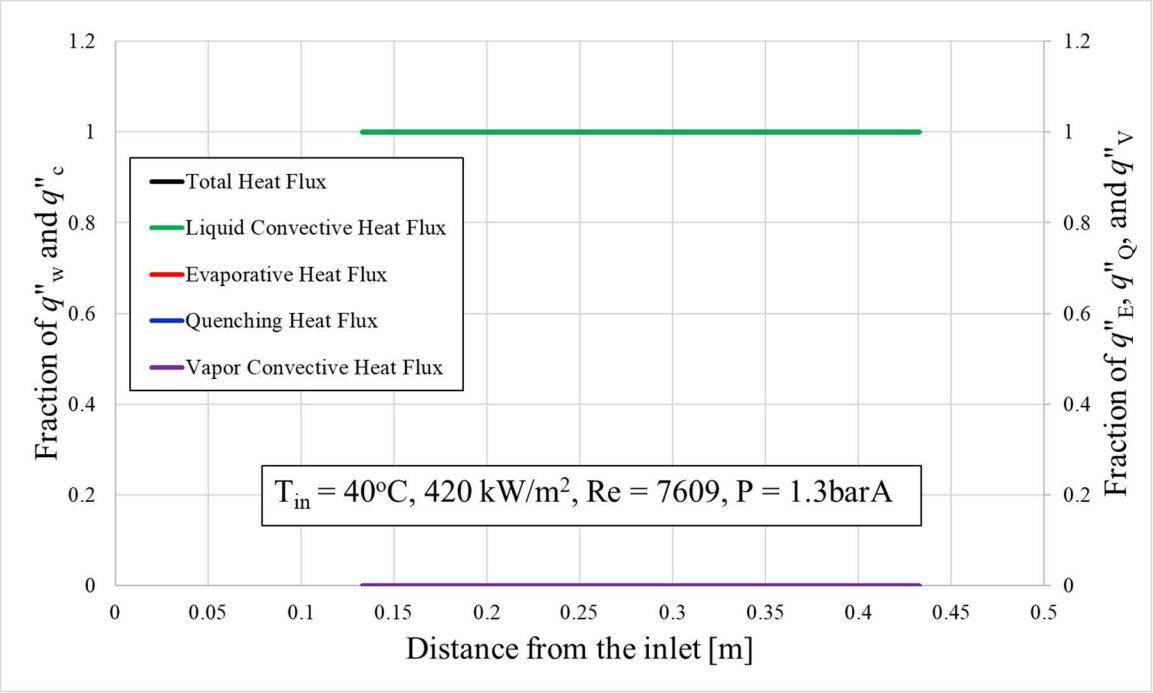

(a) Heat flux fractions for 420 kW/m^2 case

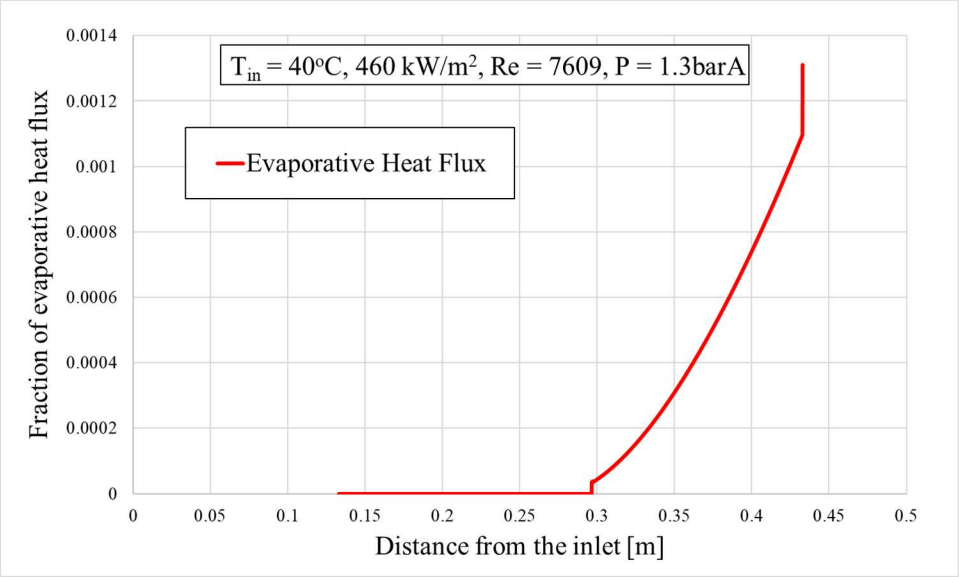

(b) Evaporative heat flux fraction for 460 kW/m^2 case

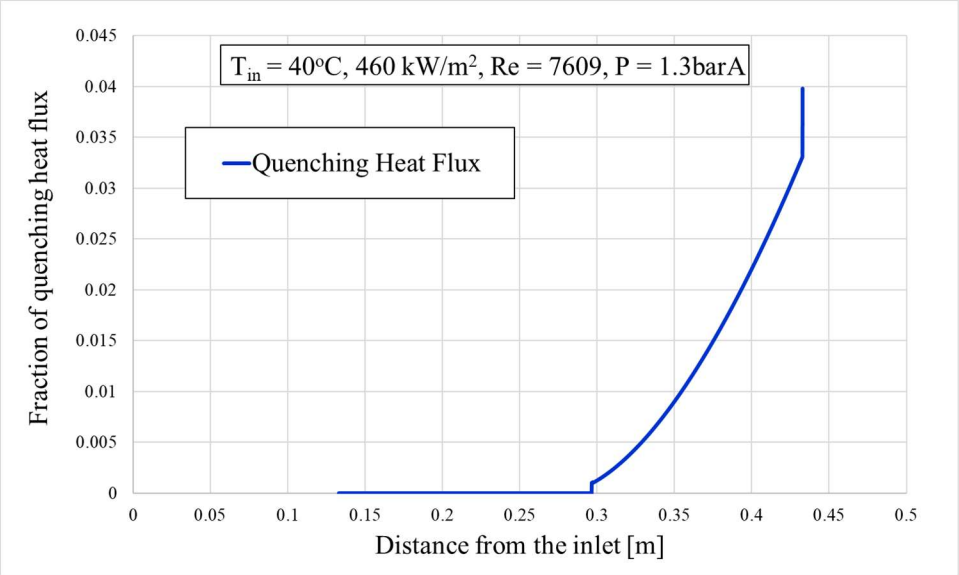

(c) Quenching heat flux fraction for 460 kW/m^2 case

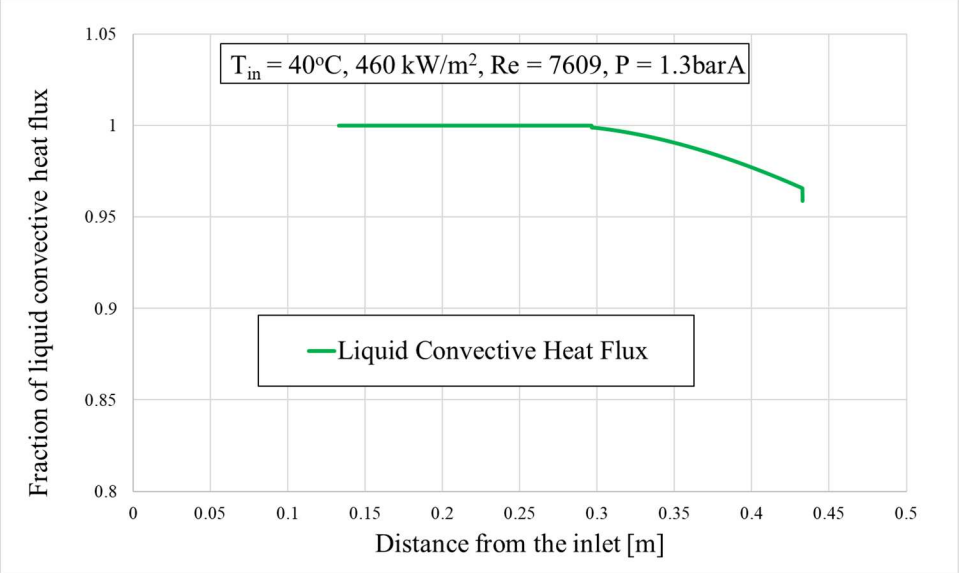

(d) Liquid convective heat flux fraction for 460 kW/m^2 case

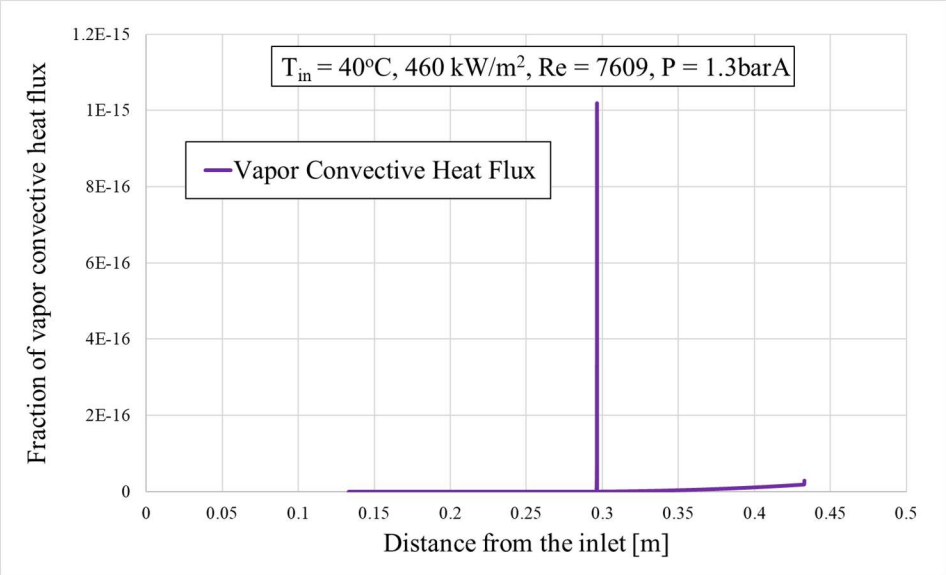

(e) Vapor convective heat flux fraction for 460 kW/m^2 case

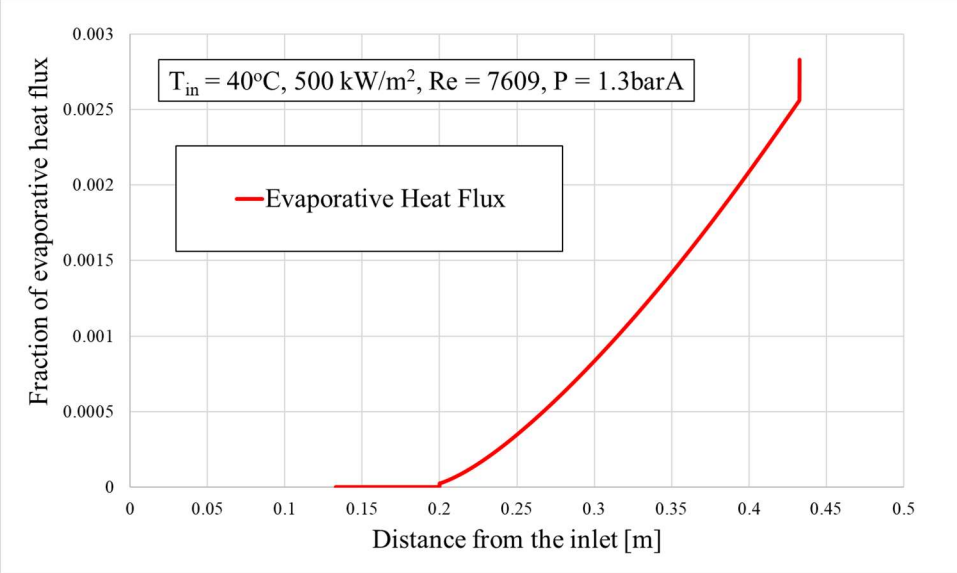

(f) Evaporative heat flux fraction for 500 kW/m^2 case

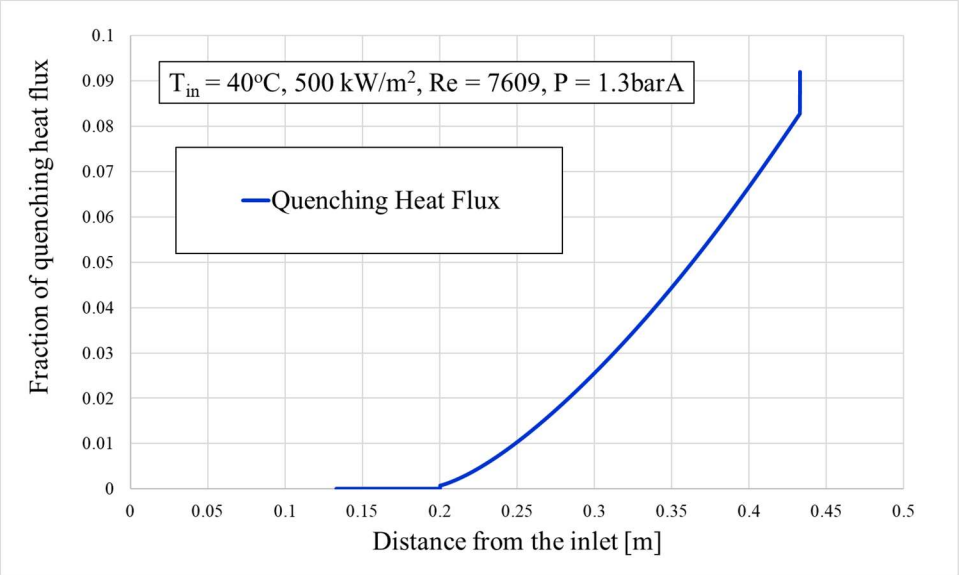

(g) Quenching heat flux fraction for 500 kW/m^2 case

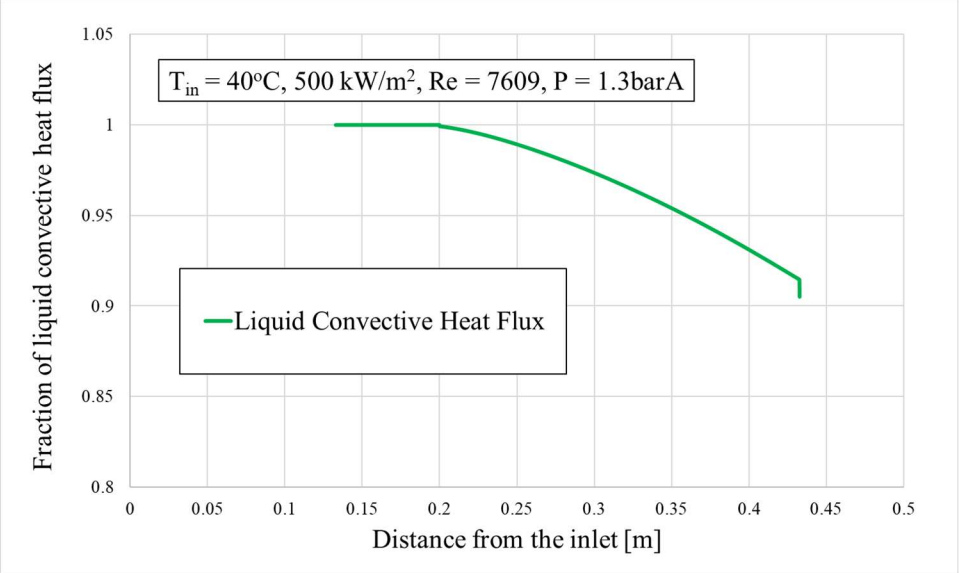

(h) Liquid convective heat flux fraction for 500 kW/m^2 case

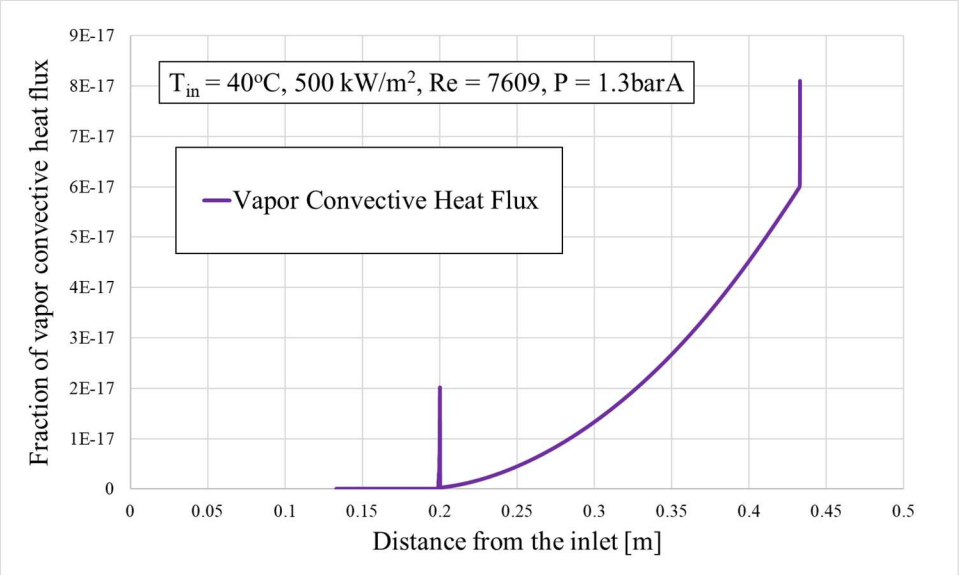

(i) Vapor convective heat flux fraction for 500 kW/m^2 case

Fig. 4 Fraction of liquid convective heat flux, evaporative heat flux, quenching heat flux, and vapor convective heat flux

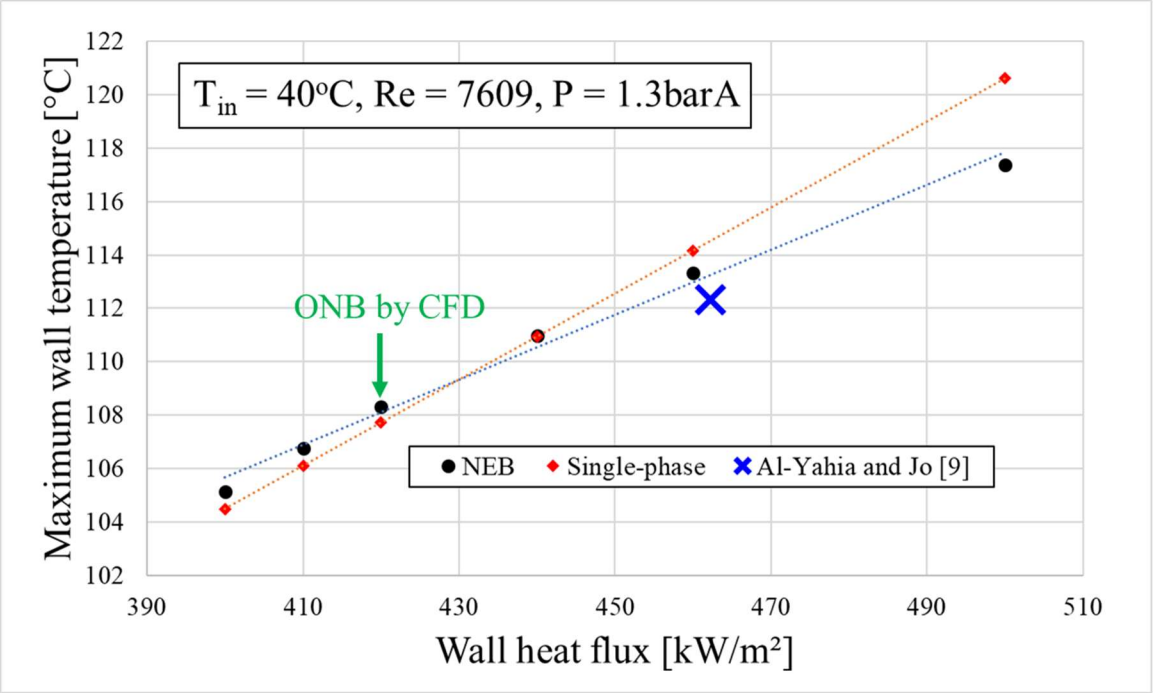
T_{in} = 40°C, Re = 7609, P = 1.3barA
ONB by CFD
NEB
Single-phase
Al-Yahia and Jo [9]
Maximum wall temperature [°C]
Wall heat flux [kW/m²]
122
120
118
116
114
112
110
108
106
104
102
390
410
430
450
470
490
510

1

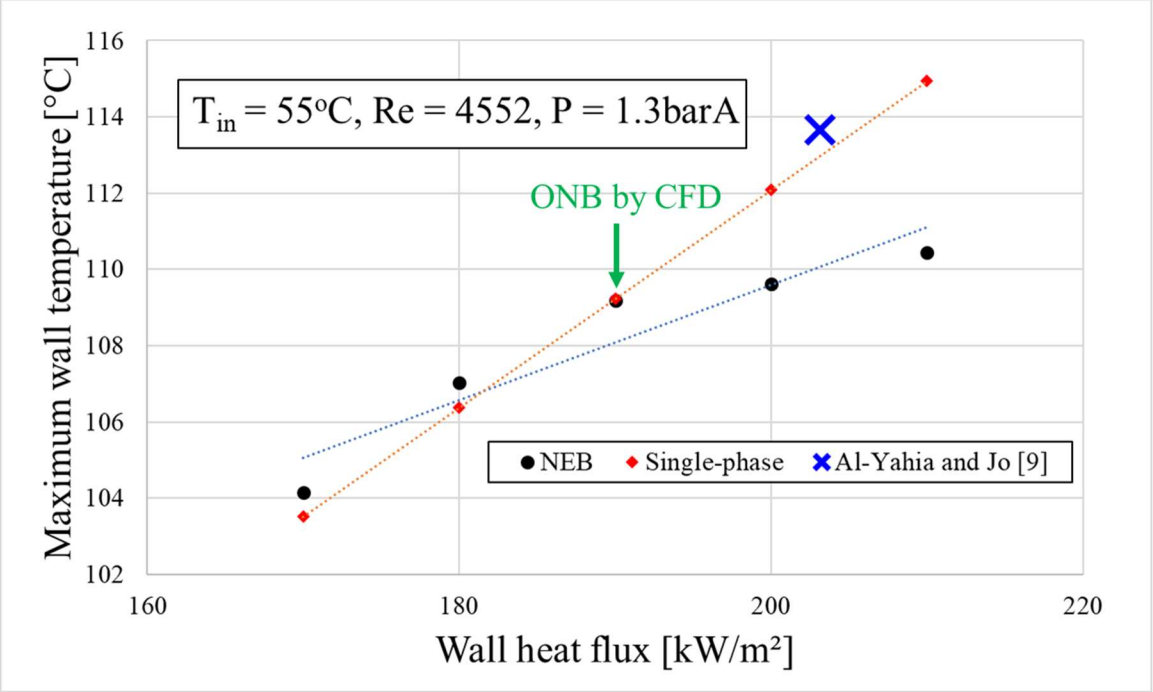
T_{in} = 55°C, Re = 4552, P = 1.3barA
ONB by CFD
NEB
Single-phase
Al-Yahia and Jo [9]
Maximum wall temperature [°C]
Wall heat flux [kW/m²]
116
114
112
110
108
106
104
102
160
180
200
220

2

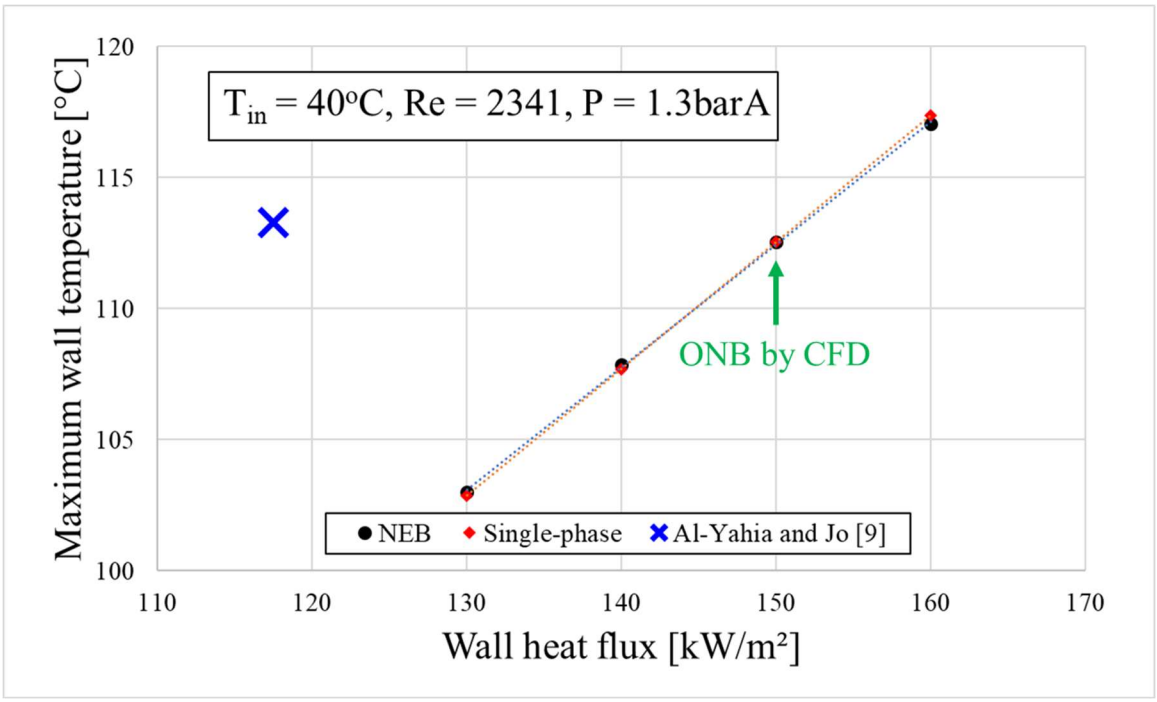

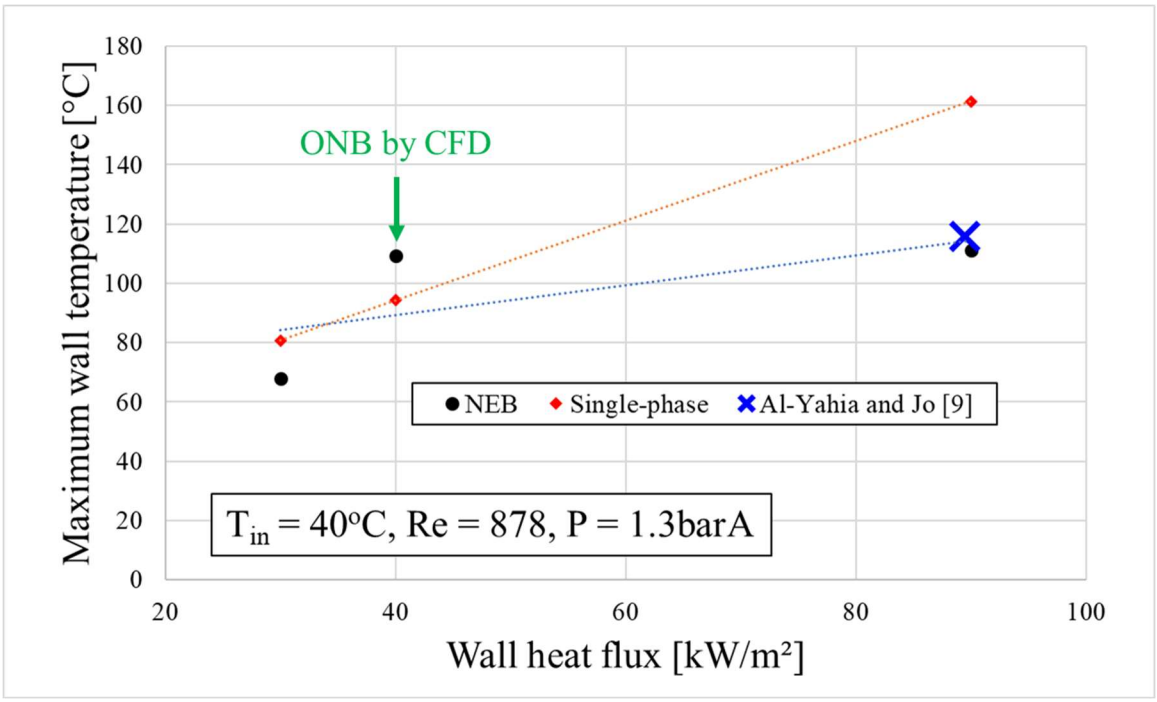

Fig. 5 ONB point prediction using single-phase CFD and NEB CFD results

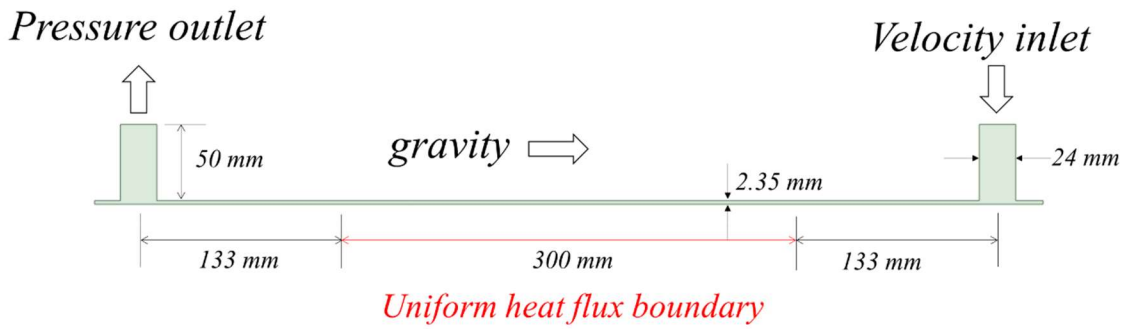

Fig. 6 Idealized actual test channel geometry in 2D

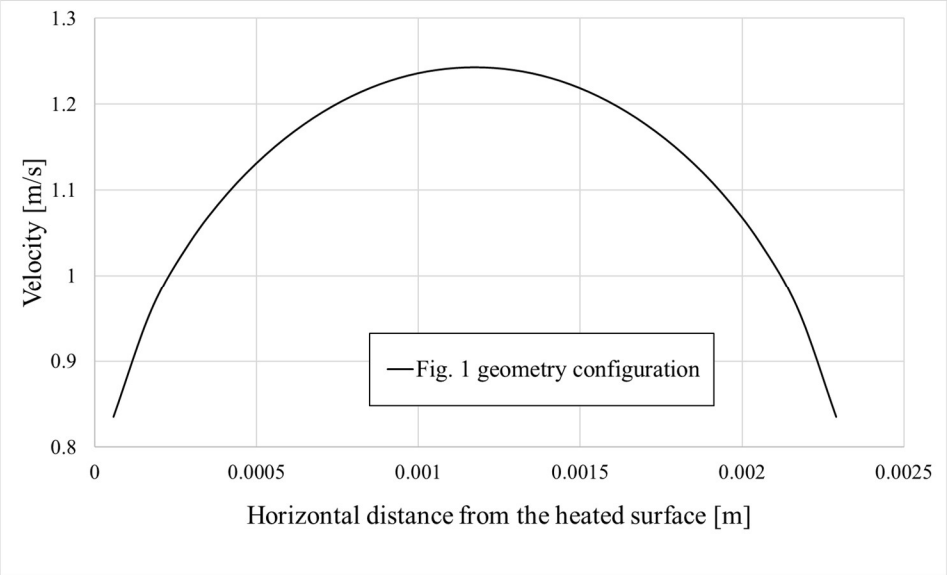

(a) Velocity profile at the heated surface starting location for Fig. 1 geometry configuration

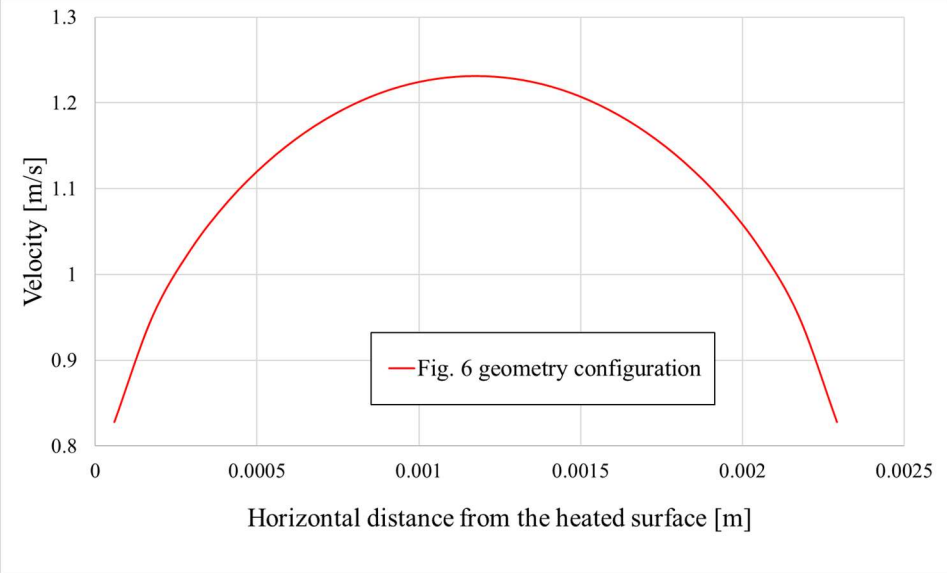

(b) Velocity profile at the heated surface starting location for Fig. 6 geometry configuration

Fig. 7 Velocity profile comparison at the heated surface starting location from two different geometries

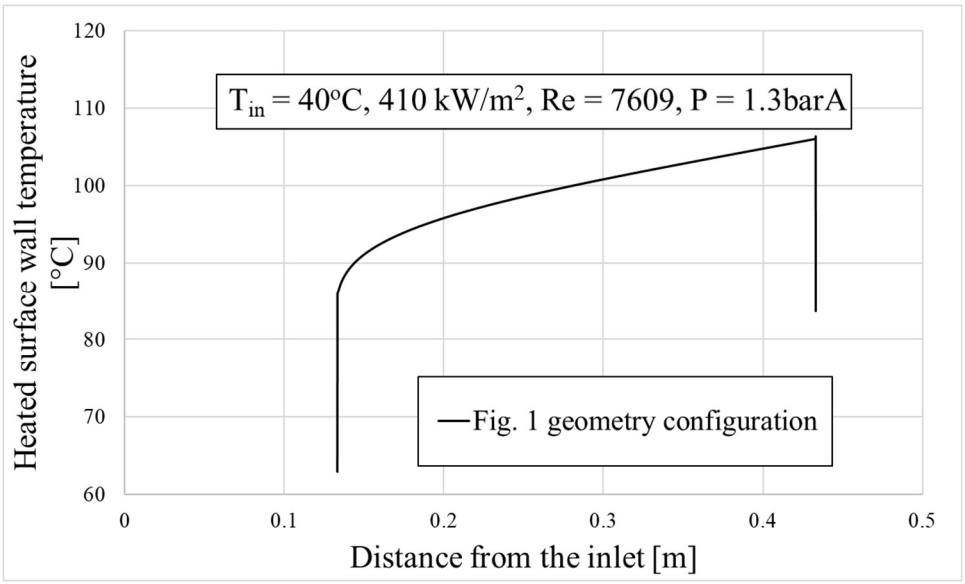

(a) Heated surface wall temperature for Fig. 1 geometry configuration

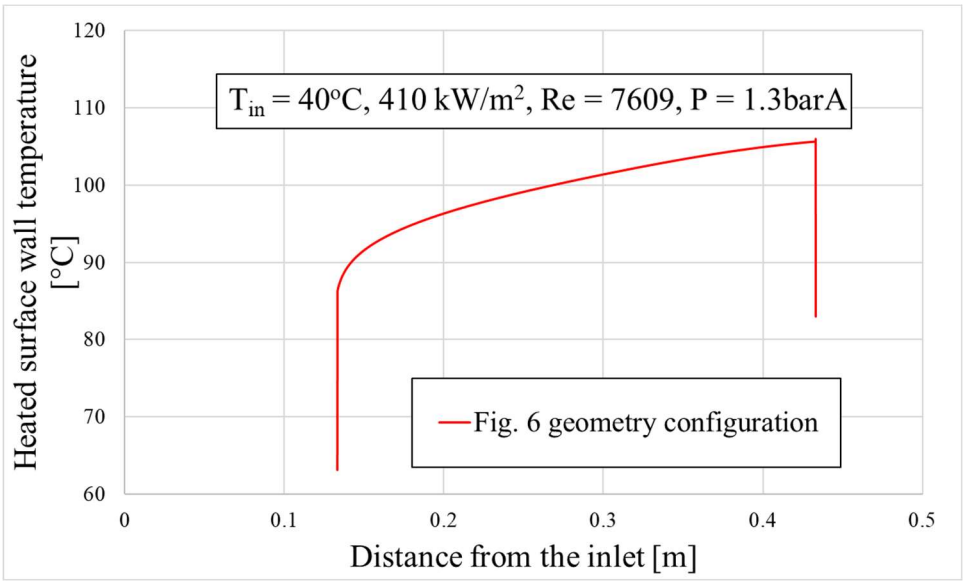

(b) Heated surface wall temperature for Fig. 6 geometry configuration

Fig. 8 Heating surface wall temperature comparison as velocity profiles